Research Article BEU Fen Bilimleri Dergisi 15(3): 1282-1292 (2026) DOI: 10.17798/bitlisfen.1890751

BİTLİS EREN UNIVERSITY
FEN BİLİMLERİ DERGİSİ
ISSN: 2147-3129 / e-ISSN: 2147-3188

3D STEP PROFILER WITH LED SOURCE AND 2D CONTINUOUS WAVELET TRANSFORM

Tahsin AYDIN [1], Mehmet KARACA [1], **Ekrem YARTAŞI** [2*]

[1] *Sivas University of Science and Technology, Department of Defense Technologies, Sivas, Türkiye*
[2] *Sivas University of Science and Technology, Department of Basic Engineering Sciences, Sivas, Türkiye*
*** Corresponding Author:** ekrem.yartasi@sivas.edu.tr

Article Info

Received: *February 16, 2026*
Revised: *June 18, 2026*
Accepted: *June 30, 2026*

Keywords

Optical Profilometry,
LED Light Source,
2D Wavelet Transform,
Gates Interferometer.

ABSTRACT

Fringe Projection Profilometry (FPP) is a widely used and reliable technique for non-contact three-dimensional (3D) surface measurements. However, when applied at micrometric and millimetric scales, its measurement accuracy may be degraded due to the limited depth of field and the speckle noise that arises in laser-based fringe patterns. In this study, a novel optical setup based on a light-emitting diode (LED) light source and a Gate's interferometer configuration is presented. The proposed system aims to reduce speckle effects by exploiting the low coherence of the LED light source. In addition, the fringe pattern is diversified by employing two beam splitters together with an additional beam-splitting element that generates a horizontal fringe structure, with the objective of enhancing the spatial resolution of the system. To the best of our knowledge, the combined use of an LED light source and two-dimensional Continuous Wavelet Transform (2D CWT) analysis within this interferometric fringe projection framework is reported for the first time in this study. The experimentally obtained phase maps are analyzed using a two-dimensional Continuous Wavelet Transform (2D CWT) method, enabling three-dimensional surface reconstruction. To evaluate the performance of the LED light source, images of the same measurement regions are also acquired using a laser light source, and a comparative analysis is performed. The comparison results indicate that, based on cross-sectional evaluations, the LED-based configuration provides, albeit limited, a reduction in noise level and an improvement in surface profile stability compared to laser-based systems

1. INTRODUCTION

Fringe projection profilometry (FPP) is widely used for acquiring three-dimensional surface topography because it enables non-contact, rapid, and high-precision measurement [1-4]. In this method, height information is extracted through phase-based calculations by analyzing the deformation of sinusoidal patterns projected onto the object surface. Owing to its simple optical configuration, high depth resolution, and low cost, accurate surface measurements can be performed at both micro- and macro-scales. For these reasons, FPP has an important role in medical applications [5,6], the automotive sector [7-9] and everyday applications [10,11].

A sinusoidal fringe pattern becomes distorted due to the deformation induced by the object's height distribution. This distortion can be interpreted as a phase shift of the illuminating light (e.g., laser or LED) that forms the interference pattern. The motivation in studies aiming to obtain non-contact three-dimensional (3D) height distributions is therefore to estimate the magnitude of this phase shift. To do so, a phase map is calculated from the captured images within the range $(-\pi, \pi]$ or $[0, 2\pi)$ using phase demodulation methods such as phase-shifting profilometry (PSP) [12,13], Fourier transform profilometry (FTP) [14,15] and continuous wavelet transform (CWT) profilometry [16-18].

In this study, an active optical profilometry approach based on FPP is presented, employing an LED illumination source and a Gates-interferometer configuration incorporating three cube beam splitters.

 License: CC BY-NC 4.0

The LED source is employed to reduce coherence-related speckle noise and improve the stability of the recorded fringe profiles. The sinusoidal intensity patterns generated by the setup were recorded on the object, and the sinusoidal analysis of the deformed fringes was performed using a two-dimensional continuous wavelet transform (2D CWT). To evaluate the performance of the LED source, additional experiments were conducted using a laser light source, and the acquired images were analyzed for comparison. Because the fringe contrast produced by LED illumination can remain limited when patterns are projected directly onto surfaces such as matte white targets, the patterns were reflected from a gridded mirror and redirected toward the camera, thereby improving image sharpness and visibility. This contrast limitation has contributed to the relatively rare use of LED sources in FPP studies.

2. MATERIAL AND METHOD

2.1. Two-dimensional Continuous Wavelet Transforms (2D CWT)

In this study, we adopt the complex Morlet wavelet as the mother wavelet because its band-pass behavior and orientation selectivity are particularly advantageous for analyzing sinusoidal fringe patterns. Under the assumption that the horizontal and vertical fringes share the same carrier spatial frequency, the intensity of the interference pattern projected onto the test surface can be expressed as in Eq. (1).

$$I(x,y) = I_0(x,y)[1 + V(x,y)\cos(2\pi f_0 x + 2\pi f_0 y + \phi(x,y))] \tag{1}$$

In this intensity formulation, $I_0(x,y)$ represents the DC (constant) illumination term, $V(x,y)$ denotes the fringe visibility (contrast), f_0 is the spatial carrier frequency, and $\phi(x,y)$ includes the phase information that encodes surface-height variations along the x- and y-directions. The 2D CWT applied to this intensity distribution is expressed in Eq. (2)

$$W(a,b,\theta) = \frac{1}{a}\iint I(x,y)\psi^*\left(\frac{x-b_x}{a}, \frac{y-b_y}{a}, r_{-\theta}\right)dxdy \tag{2}$$

In this formulation, ψ denotes the analyzing wavelet, and the superscript * indicates complex conjugation. The parameter $a > 0$ controls the analysis scale, whereas b_x and b_y represent translations along the spatial coordinates. The angle θ sets the wavelet orientation, enabling the transformation to extract directional features in the signal. The associated rotation operator $r_{-\theta}$ can be written as:

$$r_{-\theta} = \begin{bmatrix} \cos\theta & \sin\theta \\ -\sin\theta & \cos\theta \end{bmatrix} \tag{3}$$

For scale a>0, translation (b_x, b_y), and rotation angle θ, the 2-D Morlet kernel can be written as

$$\psi\left(\frac{x-b_x}{a}, \frac{y-b_y}{a}; r_{-\theta}\right) = \frac{1}{2\pi a^2} exp\{ik\frac{(x-b_x)\cos\theta + (y-b_y)\sin\theta}{a}\}exp[-\frac{(x-b_x)^2 + (y-b_y)^2}{2a^2}} \tag{4}$$

To reduce the computational cost, the transform was computed in the Fourier domain by exploiting the convolution theorem and FFTs. This approach is mathematically equivalent to performing convolution in the spatial domain; it only increases numerical efficiency while maintaining the same scale–orientation resolution. For each (a, θ) pair, the 2D CWT produces complex coefficients $W(a, \mathrm{b}, \theta)$ that represent the local fringe amplitude and phase at $\mathrm{b} = (b_x, b_y)$. Owing to the band-pass and highly directional characteristics of the complex Morlet wavelet, the response reaches its maximum when the chosen scale and orientation match the local carrier frequency and fringe direction. Accordingly, for each spatial location, the transform is evaluated over a restricted neighborhood of scales and orientations around the nominal fringe parameters, and the wrapped phase map $\phi_{\mathrm{wrap}}(x,y)$ is extracted as the argument of the coefficient with the largest magnitude, as expressed in Eq. (5):

$$\phi_{wrap}(x,y) = \arg[W(a^*, b, \theta^*)] \tag{5}$$

The 2D CWT is evaluated at each pixel, where $\mathrm{b} = (b_x, b_y)$ specifies the pixel coordinates along the x- and y-axes. For every pixel, a 2D array of complex coefficients is obtained over the scale (a) and orientation (θ) parameters. Thus, the transform of the entire image can be viewed as a four-dimensional dataset $W(a, \mathrm{b}, \theta)$. The coefficient magnitude becomes maximal at locations where the analyzing wavelet best matches the local fringe structure. These maxima, commonly termed ridge points, correspond to pixels exhibiting high coherence between the signal and the wavelet. To retrieve the phase information associated with the ridge points, the modulus $M(a, \mathrm{b}, \theta)$ of the wavelet coefficients is computed as:

$$M(a,b,\theta) = \sqrt{Im[W(a,b,\theta)]^2 + Re[W(a,b,\theta)]^2} \tag{6}$$

Ridge points are subsequently identified as the locations where this modulus attains its maximum for each pixel. The phase associated with the ridge points is then obtained by taking the argument of the corresponding complex coefficient, as given by:

$$P(a,b,\theta) = tan^{-1}\frac{Im[W(a,b,\theta)]}{Re[W(a,b,\theta)]} \tag{7}$$

In this approach, the modulus of the complex wavelet coefficients $|W(a,b,\theta)|$ is computed for each pixel, yielding a two-dimensional representation—referred to as a scalogram (see Figure 1) —as a function of scale and orientation. Each peak in the scalogram corresponds to a distinct oriented fringe component characterized by the angle θ. Equation (7) is then evaluated at the ridge points to construct the wrapped phase maps for the horizontal and vertical fringe patterns. These phase maps are subsequently unwrapped and converted into three-dimensional surface profiles using the system calibration. Finally, the two reconstructions are combined to obtain the final 3D height map of the measured object. For further details on the fringe separation procedure used in this study, see [19].

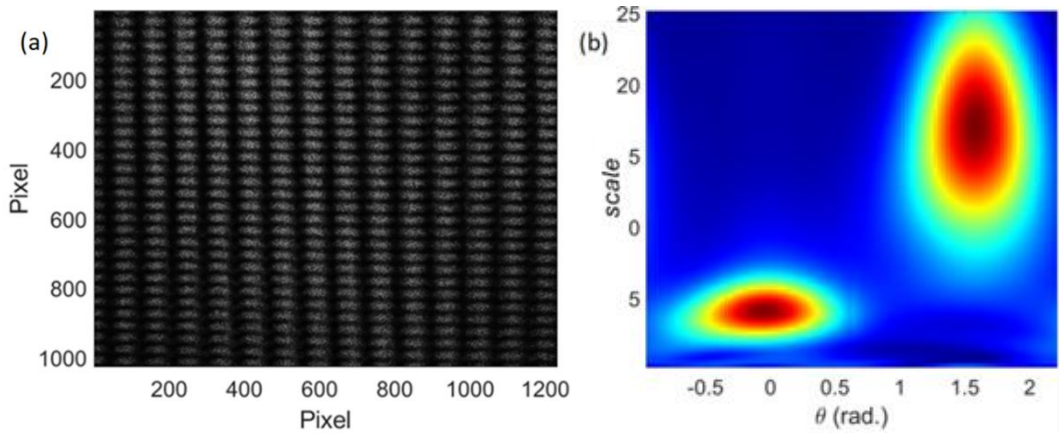


Figure 1. (a) Image of complex fringes; (b) scologram of pixel at coordinates (410,600).

Figure 1(a) presents the pixel located at coordinates (410, 600) together with its corresponding scalogram Figure 1(b). The modulus of the 2D CWT was evaluated across a range of scales and orientations to determine the optimal wavelet parameters. Two distinct maxima are observed in the scale–orientation map at different scale values and at orientations separated by approximately π/2 (≈1.5–1.6 rad), indicating that the vertical and horizontal fringe sets are mutually orthogonal. The locations of these high-intensity peaks confirm that, at this scale, the complex Morlet wavelet provides an excellent match to both fringe directions, thereby validating the spatial-frequency and orientation analysis.

Figure 1(a) shows the complex fringe image, and Figure 1(b) shows the scalogram corresponding to the pixel at (410, 600). In this scalogram, the modulus of the 2D CWT shows two distinct maxima in the

scale–orientation domain. One peak is observed near $\theta \approx 0$ rad at a scale around $a \approx 6$–7, while a second peak appears near $\theta \approx 1.5$–1.7 rad at a larger scale of approximately $a \approx 18$–20. The separation of the peak orientations by roughly $\pi/2$ indicates the presence of two fringe components that are approximately orthogonal. The concentration of energy at these peak locations also confirms that, at the corresponding scale–orientation pairs, the complex Morlet wavelet matches the local fringe structure well, supporting the reliability of the orientation and scale selection.

2.2. Optical Setup

In this study, fringe patterns that can be generated by exploiting the interferometric nature of light were investigated. To this end, an experimental setup based on a Gates interferometer was constructed. Although laser illumination is widely used in FPP, an LED source was employed in this study. A schematic representation of the proposed system is presented in Figure 2.

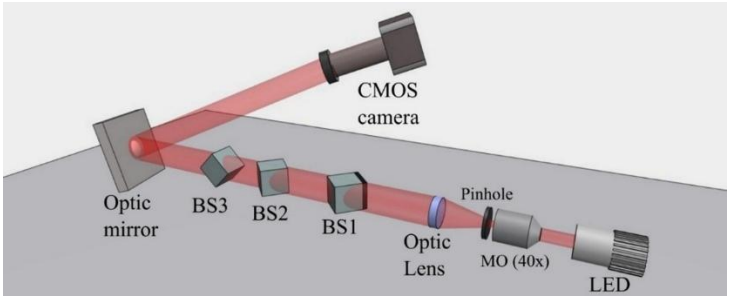


Figure 2. Schematic representation of the optical setup.

For an LED source, which is inherently incoherent, the light was first focused onto a 50 μm-diameter pinhole using a 40x microscope objective (MO) in order to suppress high-angle and irregular spatial components. This arrangement spatially filtered the LED's broad-area, multimode emission and produced a point-source-like distribution. The use of the pinhole was intended to improve the contrast and spatial regularity of the projected illumination. To collimate the light emerging from the pinhole, a plano-convex lens with a focal length of 12.5 mm was integrated into the optical setup. After collimation, a Gates interferometer configuration consisting of three beam splitters (BS) was implemented to generate square/rectangular fringe patterns.

One of the most notable advantages of the Gates interferometer configuration is that the fringe frequency of the generated interference patterns can be controlled directly through the system geometry without the need for additional optical components. The fringe frequency is defined as the number of bright or dark fringes per unit length, and it can be adjusted by rotating the beam-splitter cubes by specific angles about their axes. Increasing the rotation angle of the beam splitters leads to a higher fringe frequency, whereas decreasing the angle reduces the fringe frequency, which makes the method practical and straightforward to implement. Because the second and third beam-splitter cubes can be rotated independently about their interface planes, the fringe frequencies of the horizontal and vertical components of the interference pattern can be tuned separately, enabling flexible generation of two-dimensional fringe patterns. In addition, the Gates interferometer offers flexibility in the choice of illumination source and can operate with both laser and LED sources; in particular, the use of low-coherence LED illumination can significantly reduce speckle noise, which can limit measurement resolution in laser-based systems [20].

The structured illumination patterns were initially recorded by projecting them directly onto the test object. However, the fringes could not be captured with sufficient contrast and sharpness, which was attributed to the limited sensitivity of the CMOS camera and the surface reflectance characteristics. Therefore, an alternative acquisition strategy was adopted to improve fringe visibility and to assess the phase-retrieval performance of the system. A silicon-based calibration mirror from a Filmetrics Profilm 3D system (Figure 3) was used to reflect the structured light directly onto the camera sensor. The mirror has a step height of 9.15 μm, as reported by the manufacturer [21]. Owing to the regular microstructures on the mirror surface, the fringe variations were recorded with high contrast. The images were transferred to MATLAB for phase analysis, and 3D topographies were reconstructed.



Figure 3. A silicon-based calibration mirror.

In the LED-based setup, separate reference images could not be acquired because of the limited measurement area and practical constraints. Instead, the reference surface was estimated from the data. A nominally flat region was selected in the unwrapped phase map, and a surface-fitting procedure was used to define the reference plane. The fitted reference was then extended over the full field to obtain the final height distribution.

3. RESULTS AND DISCUSSION

3.1. Comparison of LED and Laser Illuminated Interference Pattern

Figure 4 compares the fringe patterns and the corresponding intensity profiles acquired under LED and laser illumination. The LED results are presented in Figure 4(a), where the fringe pattern appears relatively regular and the extracted horizontal and vertical line profiles exhibit a modulation that is generally closer to a sinusoidal shape, although the fringes appear somewhat less sharp. The laser results are shown in Figure. 4(b), where the fringe features appear sharper, while speckle-related fluctuations and local intensity variations are more noticeable, leading to more irregular line profiles. Overall, this comparison indicates that the illumination source can influence fringe visibility, apparent sharpness, and the smoothness of the recorded intensity signals, which may, in turn, affect subsequent phase-demodulation performance.

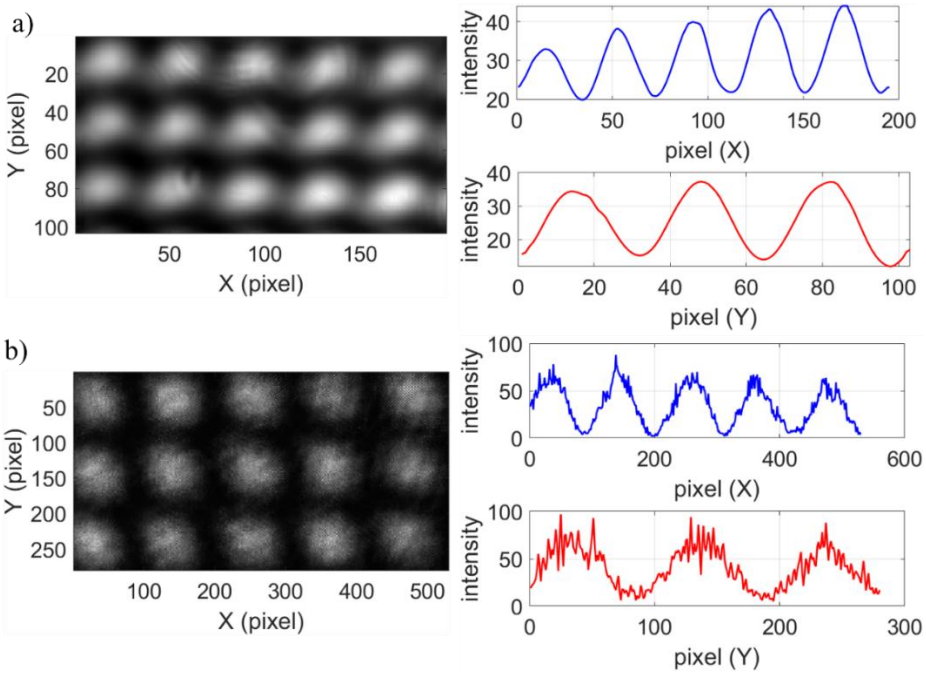


Figure 4. Fringe patterns and intensity cross-sections recorded with LED (a) and laser (b) illumination.

Figures 5(a) and 5(b) comparatively present the fringes acquired from the same measurement region using LED and laser illumination. Under LED illumination, the fringe pattern exhibits relatively lower contrast, whereas the bright–dark transitions appear smoother and more uniform. Under laser illumination, the contrast increases noticeably; however, speckle effects are also observed, likely due to the high spatial coherence of the laser and the fact that the measurement surface may not be perfectly flat. In both cases, the diagonal boundary corresponding to the inclined step region remains clearly visible, indicating that the fringe patterns reflect the surface topography consistently. Overall, these results suggest that, while laser illumination provides a contrast advantage, it may introduce speckle-related noise, whereas LED illumination can still yield a measurable fringe pattern despite lower contrast and a slight degradation in fringe orthogonality.

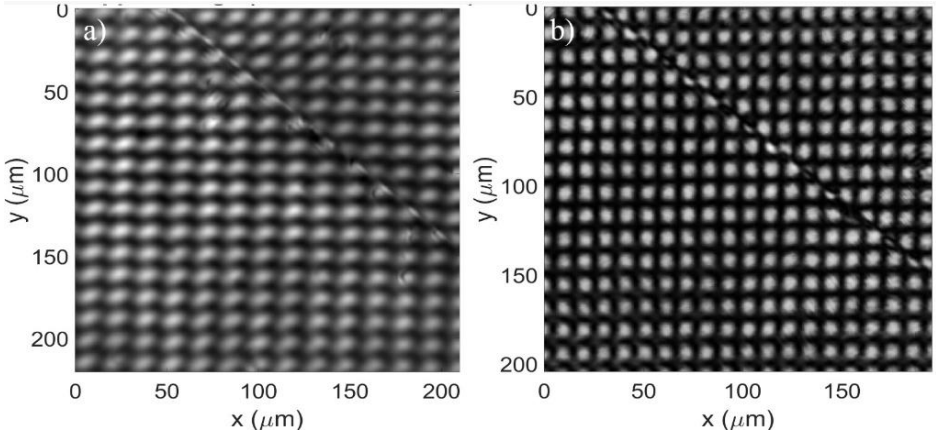


Figure 5. Complex fringes acquired from the same measurement region with LED source (a) and laser source (b).

3.2. Three-Dimensional (3D) Surface Reconstruction

The specimen is illuminated by an approximately collimated fringe field; therefore, the recorded fringe pattern undergoes negligible horizontal or vertical scaling. Under these conditions, a numerical reference surface is estimated from the measurement itself, since acquiring a physical reference surface is experimentally difficult under the present constraints. Specifically, a nominally flat and feature-free region, selected to be as independent of the sample topography as possible, is identified on the unwrapped phase map, and a surface-fitting procedure is applied to this region. The fitted surface is then extended over the full field of view and used as the reference surface.

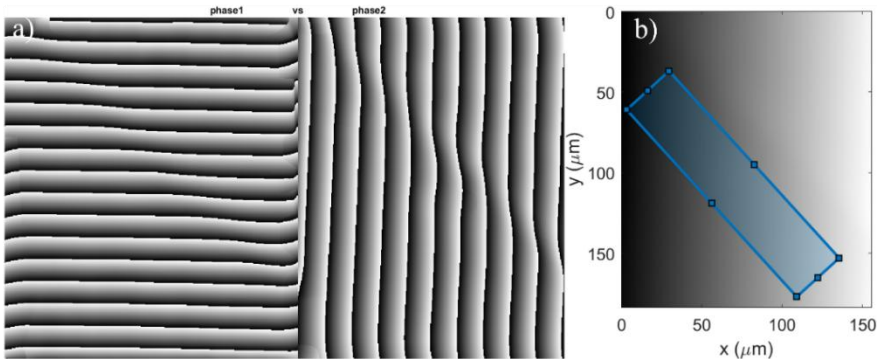


Figure 6. Horizontal and vertical wrapped phase profiles (a); selection of the fitting region (b) from the same area for reference-surface estimation

This approach is also motivated by experimental configuration: the structures generating the fringes are etched on the mirror, so their positions cannot be changed, and the fringe frequency and location can only be adjusted within a limited range. By compensating the system-related phase components using the estimated reference surface, the remaining phase distribution corresponds primarily to the specimen

surface. For clarity, the measurement region corresponding to the wrapped phase profile in Figure 6(a) and the region used for surface fitting in Figure 6(b) are indicated so that both phase profiles refer to the same field of view.

Surface profiles obtained using the LED illumination source with the double-fringe configuration are presented in Figure 7. In the upper row, Figure 7(a) shows, from left to right, the horizontal, vertical, and superimposed 3D reconstructions in a top-view representation, illustrating the overall trend of the surface geometry and the step structure. Compared to single-direction fringe patterns, the double-fringe configuration appears to partially reduce orientation-dependent periodic ripples mapped onto the reconstructed surface, enabling a more balanced reconstruction.

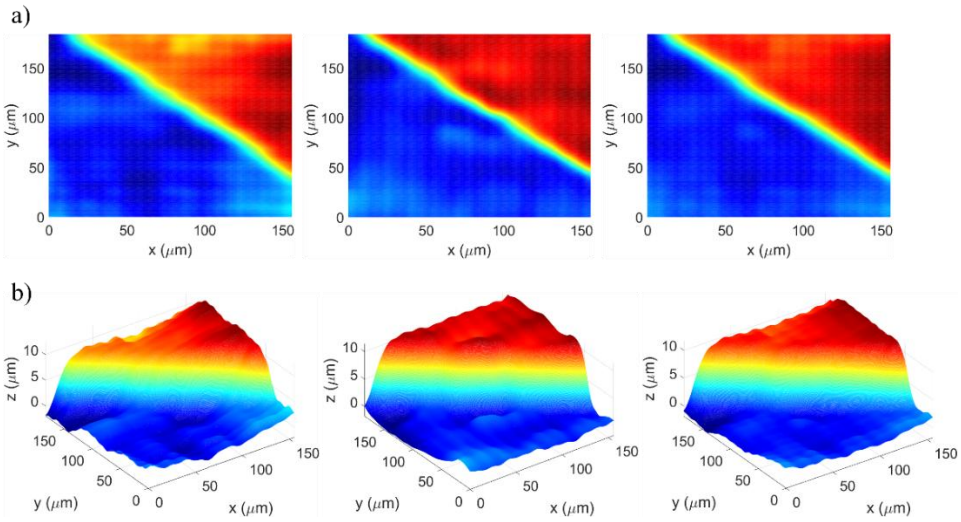


Figure 7. From left to right: horizontal, vertical, and superimposed 3D surface reconstructions obtained with the LED-based configuration (a); the corresponding oblique 3D views are shown from left to right in the same order (b).

The oblique three-dimensional views in the lower row (Figure 7(b)) reveal the overall surface topography, and they suggest continuous step transitions with a relatively uniform distribution of height differences. Nevertheless, the limited fringe contrast associated with the low-coherence nature of LED illumination may prevent low-amplitude fluctuations from being completely eliminated. Despite this, by combining the bidirectional information provided by the double-fringe approach, the surface profile in the LED-based measurements can be obtained with overall micrometer-scale consistency.

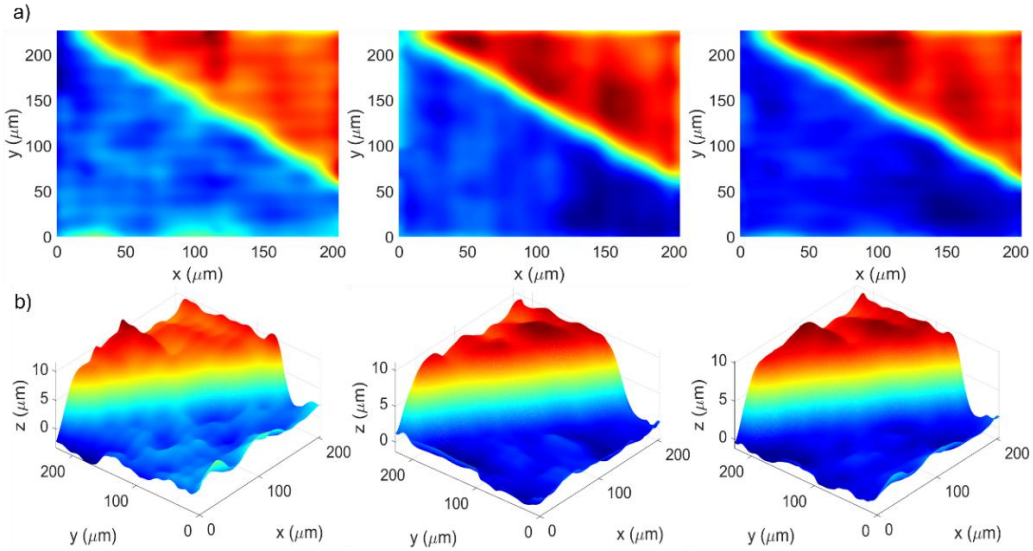


Figure 8. From left to right: horizontal, vertical, and superimposed 3D surface reconstructions obtained with the laser-based configuration (a); the corresponding oblique 3D views are shown from left to right in the same order (b).

Surface profiles obtained using laser illumination in the double-fringe configuration are shown in Figure 8, acquired by reproducing the same optical setup used for the LED-based measurements. In the height maps presented in Figure 8(a), the overall trend of the surface geometry can be observed, and the higher fringe contrast allows surface transitions to be represented with sharper boundaries. However, due to the high coherence of the laser source, irregularities and low-amplitude noise components, attributed to speckle effects, are noticeable in certain regions of the reconstructed surface. The three-dimensional profiles in Figure 8(b) clearly reveal the general surface topography; nevertheless, local fluctuations, likely associated with speckle, remain difficult to suppress, particularly in regions expected to be relatively smooth. While the double-fringe approach can partially reduce orientation-dependent harmonic effects compared to single-direction fringes, coherence-related noise appears to remain a contributing factor in laser-based surface reconstruction. Finally, cross-sectional profiles extracted from selected regions were used to further examine and detail the surface characteristics.

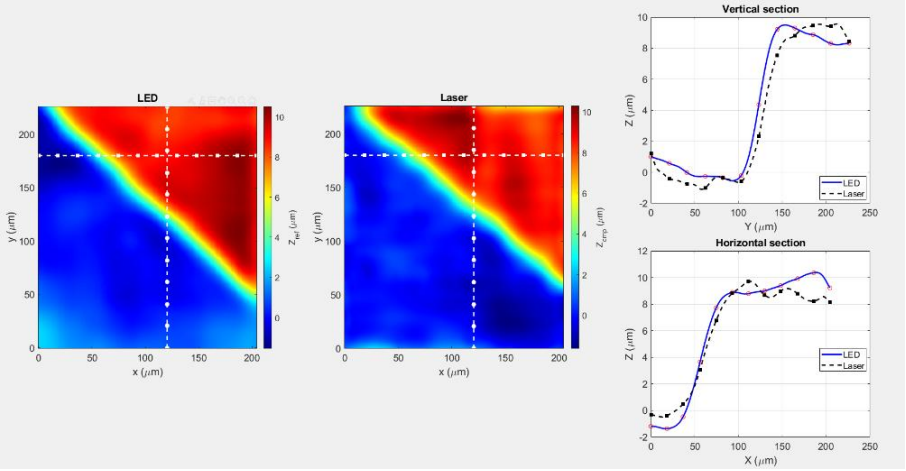


Figure 9. Cross-sectional comparison of the laser double-fringe and LED double-fringe profiles.

A comparison of the surface profiles obtained using the double-fringe approach under laser and LED illumination is presented in Figure 9. In both configurations, the overall surface geometry and the stepped structure can be reconstructed in a similar manner.

In the laser-based measurements, local fluctuations attributed to speckle are more evident in the reconstructed surface profile compared to the LED result, likely due to the higher coherence of the laser source. In the LED-based double-fringe configuration, the speckle effect appears relatively weaker; however, the limited fringe contrast associated with lower coherence can make it difficult to fully suppress low-amplitude variations on the reconstructed surface. Based on the recorded images, it can be suggested that the relatively speckle-reduced nature of the LED profile may offer an advantage for profilometry measurements.

Table 1. Reconstruction error comparison for single and double directional fringe patterns

	LED based configuration with single-directional fringes	**LED based configuration with double-directional fringes**
ME (µm)	0.399	0.261
MAE (µm)	0.489	0.444
RMSE (µm)	0.596	0.544
MAPE (%)	5.35	4.85

The performance of the proposed configurations was evaluated using a reference mirror with a known height of 9.15 µm. The reconstructed surface data were processed in MATLAB by considering this value as the ground truth, and the corresponding error metrics were calculated. As shown in Table 1, the LED-

based configuration with double-directional fringe patterns yields lower error values compared to the single-directional case. In particular, improvements are observed across all metrics, including mean error-ME (from 0.399 μm to 0.261 μm); mean absolute error, MAE (from 0.489 μm to 0.444 μm); root mean square error, RMSE (from 0.596 μm to 0.544 μm); and mean absolute percentage error, MAPE (from 5.35% to 4.85%). These results indicate that the use of double-directional fringes enhances reconstruction accuracy and reduces both systematic and random errors. The observed improvement is attributed to the reduced sensitivity to direction-dependent fluctuations, achieved by averaging the measurements obtained from horizontal and vertical fringe directions rather than relying on a single orientation. This approach reduces orientation-dependent effects and leads to a more stable and reliable surface reconstruction.

The experimental setup was optimized to address the inherent limitations of LED illumination, specifically the lower fringe contrast and restricted acquisition area. To maintain high measurement stability, the fringes were projected onto a reference mirror with a known step-height. This configuration required a direct reflection path into the camera sensor, making the system highly sensitive to optical alignment. Any displacement of the camera or the object led to significant shifts in fringe patterns or loss of intensity, primarily due to the low coherence of the LED source. Furthermore, even microscopic surface imperfections on the reference mirror were observed to affect the quality of the reference image. Therefore, the current measurement area was constrained to ensure the reliability and precision of the acquired data under these physical conditions.

Due to the lower temporal coherence of LED sources, the recorded fringe contrast decreases compared with laser illumination. In the 2D-CWT phase retrieval process, this reduced modulation depth may attenuate weak high-spatial-frequency phase variations, which can lead to smoother reconstructed topographies and reduced low-amplitude fluctuations, as observed in the LED-based reconstruction in Fig. 7. In contrast, laser illumination provides higher fringe contrast and therefore higher sensitivity to small phase variations, as shown in Fig. 8. However, these small variations may include both fine surface details and coherent noise components, particularly speckle-related fluctuations. The cross-sectional comparison in Fig. 9 supports this interpretation: the laser-based profile retains stronger local fluctuations, whereas the LED-based profile exhibits a smoother response with reduced fluctuation amplitudes. These results highlight the inherent trade-off between noise robustness and fine-detail sensitivity when selecting the illumination source.

4. CONCLUSION AND SUGGESTIONS

In this study, a structured-light profilometry approach based on a Gates interferometer was implemented using an LED illumination source, and the feasibility of wavelet-transform-based phase analysis with a double-fringe pattern was experimentally demonstrated, to the best of our knowledge, for the first time. In the proposed setup, phase information was extracted from LED-generated interference patterns using two-dimensional (2D) continuous wavelet transforms (CWT), and three-dimensional surface (mesh) reconstructions were obtained from the resulting absolute phase profiles. The results indicate that the wavelet-transform approach, which is commonly adopted in laser-based systems, can also be applied with a low-coherence source such as an LED. To examine one of the main motivations for using LED illumination, reduced speckle effects, measurements were additionally acquired from the same region using a laser source and comparatively evaluated.

Within the scope of the study, measurements were performed on regions containing an inclined step geometry, and such sharp height variations were observed to be represented effectively by the wavelet-transform-based analysis. For reconstructions obtained from single-direction interference patterns, orientation-dependent harmonics were found to be mapped onto the reconstructed surface. By contrast, when the horizontal and vertical fringe patterns were jointly employed in the double-fringe approach, these direction-dependent harmonics were partially suppressed, yielding a more balanced representation of the surface topography. In future work, numerical simulations based on synthetic fringe patterns with known height distributions will also be performed to further evaluate the 2D-CWT phase retrieval model under controlled fringe contrast, noise and speckle conditions, and to compare the simulated reconstructions with experimental measurements.

The presented cross-sectional analyses were performed using selected individual profiles and are intended to examine the local behavior of the surface reconstruction. Although the extracted profiles allow a qualitative comparison of how different fringe configurations influence the surface representation, these results cannot be regarded as a generalizable performance assessment for the entire surface. The cross-sectional profiles can reveal method-specific differences, especially around step transitions and local fluctuations, but they provide limited insight into the overall accuracy and the spatial distribution of errors across the full field. Therefore, as a complement to the cross-sectional evaluation, more comprehensive quantitative error analyses based on the full-field quantitative comparisons between LED- and laser-based reconstructions are planned in future work. to enable a more complete performance assessment.

Acknowledgements

This research was carried out with the financial support of the Scientific and Technological Research Council of Türkiye (TÜBİTAK), within the scope of Project No. 123F413

Conflict of Interest Statement

There is no conflict of interest between the authors.

Statement of Research and Publication Ethics

The study is complied with research and publication ethics.

Artificial Intelligence (AI) Contribution Statement

The authors declare that this manuscript was written and analyzed by the authors. Language editing assistance was used; however, the scientific content, data analysis, and figures are entirely the authors' own work

Contributions of the Authors

T. Aydın contributed to the experiments performed, the literature review, and the evaluation of the results obtained. M. Karaca contributed to the experiments and the evaluation of the results obtained. E. Yartaşı contributed to the experimental design, the execution of the experiments and the writing of the manuscript.

REFERENCES

[1] Z. Wang, "Review of real-time three-dimensional shape measurement techniques," May 01, 2020, Elsevier B.V. doi: 10.1016/j.measurement.2020.107624.

[2] S. Zhang, "Recent progresses on real-time 3D shape measurement using digital fringe projection techniques," *Opt. Lasers Eng.*, vol. 48, no. 2, pp. 149–158, Feb. 2010, doi: 10.1016/j.optlaseng.2009.03.008.

[3] S. Zhang, "High-speed 3D shape measurement with structured light methods: A review," Jul. 01, 2018, Elsevier Ltd. doi: 10.1016/j.optlaseng.2018.02.017.

[4] S. Zhang and S. Lei, "Flexible 3-D shape measurement using projector defocusing," *Optics Letters*, Vol. 34, Issue 20, pp. 3080-3082, vol. 34, no. 20, pp. 3080–3082, Oct. 2009, doi: 10.1364/OL.34.003080.

[5] H. Chen et al., "Color structured light system of chest wall motion measurement for respiratory volume evaluation," *J. Biomed. Opt.*, vol. 15, no. 2, p. 026013, 2010, doi: 10.1117/1.3368680.

[6] R. Zuo et al., "Deep-learning-based endoscopic single-shot fringe projection profilometry," *J. Biomed. Opt.*, vol. 30, no. 08, Aug. 2025, doi: 10.1117/1.jbo.30.8.086003.

[7] A. Castriota, M. De Giorgi, F. Manco, A. Morabito, and R. Nobile, "A semi-automatic methodology for tire's wear evaluation," *Measurement and Control (United Kingdom)*, vol. 56, no. 7–8, pp. 1292–1307, Sep. 2023, doi: 10.1177/00202940221098051.

[8] L. Hinz et al., "Fringe projection profilometry in production metrology: A multi-scale comparison in sheet-bulk metal forming," *Sensors*, vol. 21, no. 7, Apr. 2021, doi: 10.3390/s21072389.

[9] A. Lakshman S, F. Delzendehrooy, B. Balasubramaniam, G. E Kremer, Y. Liao, and B. Li, "Corrosion characterization of engine connecting rods using fringe projection profilometry and unsupervised machine learning," *Meas. Sci. Technol.*, vol. 35, no. 8, Aug. 2024, doi: 10.1088/1361-6501/ad4dd1.

[10] G. S. Spagnolo, L. Cozzella, and F. Leccese, "Projected Fringes Profilometry for Cultural Heritage Studies."

[11] G. S. Spagnolo, L. Cozzella, and F. Leccese, "Fringe-projection profilometry for recovering 2.5D shape of ancient coins," *Acta IMEKO*, vol. 10, no. 1, pp. 142–149, 2021, doi: 10.21014/ACTA_IMEKO.V10I1.872.

[12] G. Kösoğlu, H. Yüksel, and M. N. Inci, "Phase stepping optical profilometry using fiber optic Lloyd's mirrors," *Appl. Opt.*, vol. 55, no. 4, p. 846, Feb. 2016, doi: 10.1364/ao.55.000846.

[13] A. Novack, D. D'Annunzio, E. D. Çubuk, N. Inci, and L. Molter, "Three-dimensional phase step profilometry with a multicore optical fiber," *Applied Optics*, Vol. 51, Issue 8, pp. 1045-1048, vol. 51, no. 8, pp. 1045–1048, Mar. 2012, doi: 10.1364/AO.51.001045.

[14] K. Bulut and M. N. Inci, "Three-dimensional optical profilometry using a four-core optical fibre," *Opt. Laser Technol.*, vol. 37, no. 6, pp. 463–469, Sep. 2005, doi: 10.1016/j.optlastec.2004.07.005.

[15] T. Kart, G. Kösoğlu, H. Yüksel, and M. N. İnci, "Fourier transform optical profilometry using fiber optic Lloyd's mirrors," *Appl. Opt.*, vol. 53, no. 35, p. 8175, Dec. 2014, doi: 10.1364/ao.53.008175.

[16] M. A. Gdeisat, D. R. Burton, and M. J. Lalor, "Spatial carrier fringe pattern demodulation by use of a two-dimensional continuous wavelet transform," *Appl. Opt.*, vol. 45, no. 34, pp. 8722–8732, Dec. 2006, doi: 10.1364/AO.45.008722.

[17] A. Inanç, G. Kösoğlu, H. Yüksel, and M. Naci Inci, "3-D optical profilometry at micron scale with multi-frequency fringe projection using modified fibre optic Lloyd's mirror technique," *Opt. Lasers Eng.*, vol. 105, pp. 14–26, Jun. 2018, doi: 10.1016/j.optlaseng.2017.12.012.

[18] J. Ma, Z. Wang, B. Pan, T. Hoang, M. Vo, and L. Luu, "Two-dimensional continuous wavelet transform for phase determination of complex interferograms," 2011.

[19] K. Patorski and K. Pokorski, "Separation of complex fringe patterns using two-dimensional continuous wavelet transform," *Applied Optics*, Vol. 51, Issue 35, pp. 8433-8439, vol. 51, no. 35, pp. 8433–8439, Dec. 2012, doi: 10.1364/AO.51.008433.

[20] J. R. Sánchez, A. Martínez-García, J. A. Rayas, and M. León-Rodríguez, "LED source interferometer for microscopic fringe projection profilometry using a Gates' interferometer configuration," *Opt. Lasers Eng.*, vol. 149, Feb. 2022, doi: 10.1016/j.optlaseng.2021.106822.

[21] KLA, "Step Height Standards." *Accessed: Feb. 10*, 2026. [Online]. Available: https://www.kla.com/products/instruments/filmetrics-accessories/step-height-standards